Toward realistic dynamics of rotating orbital debris and implications for light curve interpretation

Gregory W Ojakangas
Drury University

Nicole Hill
ESCG/MEI Technologies

ABSTRACT

Optical observations of rotating space debris near GEO contain important information on size, shape, composition, and rotational states, but these aspects are difficult to extract due to data limitations and the high number of degrees of freedom in the modeling process. For tri-axial rigid debris objects created by satellite fragmentations, the most likely initial rotation states have large components of angular velocity directed along the intermediate axis of inertia, leading to large reorientations of the body on the timescale of the rotation period. This lends some support to the simplest possible interpretation of light curves -- that they represent sets of random orientations of the objects of study, although such rotation states do not typically sample orientation space uniformly even over a large number of rotations. Furthermore, effects of solar radiation can cause significant modification of rotation states within timescales of hours, for cm-sized objects of irregular shape. In order to examine the rotational dynamics under solar influence, a set of seven first-order coupled equations of motion were assembled in state form: three are Euler equations describing the rates of change of the components of angular velocity in the body frame, and four describe the rates of change of the components of the unit quaternion. Quaternions are four-dimensional extensions of complex numbers that form a seamless, singularity-free representation of body orientation on S3. The Euler equations contain explicit terms describing torque from solar radiation. Numerical integrations reveal widely varying rotation states, such that in general, light curves for small objects of irregular shape can be expected to radically change character between different observation epochs. Because the axis of maximum rotational inertia tends to be roughly coincident with the normal to the largest projected cross-sectional area, internal friction or magnetic damping, if significant, may lead to reduced variation of light curve amplitudes at a given phase angle, but a large dependence of the amplitudes on phase angle. At a given phase angle, databases are generated that show reflected intensities at all orientations simultaneously, within a semi-transparent 3D spherical projection of the quaternion intensity database. Simulated rotational sequences form trajectories through this space which may be conveniently visually examined relative to all possible orientations. Symmetries in the problem suggest that if internal friction or magnetic retarding torques are significant, preferred rotation states will be likely, defined relative to the object-sun direction and/or the magnetic field direction in inertial space and relative to the maximum principal axis of inertia in the body coordinate system. Such rotation states may greatly simplify the problem of light curve interpretation by reducing the number of degrees of freedom in the problem. Acknowledgements: This work was produced under NASA contract NNJ05HI05.

1. Introduction

In recent years, observation and analysis of unresolved light curves from orbiting debris objects has increased and advanced considerably, as the importance of these data for understanding the on-orbit debris population has come into focus. However, as more data have been gathered, it has become evident that the light curves of individual objects can change character quite rapidly, particularly for small objects in GEO with high area-to-mass ratios [1],[2]. Here we report that a likely cause of such variations is a rapidly evolving rotation state due to the torque caused by solar radiation pressure acting on irregularities in shape and/or reflectivity. In order to study these effects, geometric models of fragments produced by earth-based satellite impact tests and other objects believed to accurately represent orbital debris are created with a laser scanner at the Orbital Debris Program Office at the Johnson Space Center (JSC) [3]. These are employed in a MATLAB code that can simulate realistic rotational dynamics and consequent light curves. The simulations may be compared with data acquired by telescope or simulated in the Optical Measurements Center (OMC) at JSC using a CCD camera and an artificial light source incident upon the fragments themselves as they are gripped and rotated using a robotic arm.

2. Probable initial conditions

The initial rotational conditions imparted to a debris object upon injection into orbit are generally unknown, but under plausible assumptions it is possible to compute a distribution of initial rotational states in a probabilistic manner. These assumptions are (1) upon creation during an on-orbit breakup, a debris object is originally oriented randomly relative to the fragmenting parent body, and (2) the object receives an initial impulse that is applied at a random location on the object from the side facing the parent body. Under these assumptions, the distribution of probable initial angular velocity vectors can be readily computed. The force producing the initial rotation is given by F, which acts over a time Δt on the jth area element of the modeled object, for which the position vector is $\mathbf{r_j}$. The unit vector from the facet toward the parent body is given by $\mathbf{n_p}$. Since the initial angular velocity is zero and the force acts as a short impulse, the imparted angular momentum is given by

$$\vec{L} = -F\Delta t\left[\vec{r}_j \times \vec{n}_p\right] \qquad (1)$$

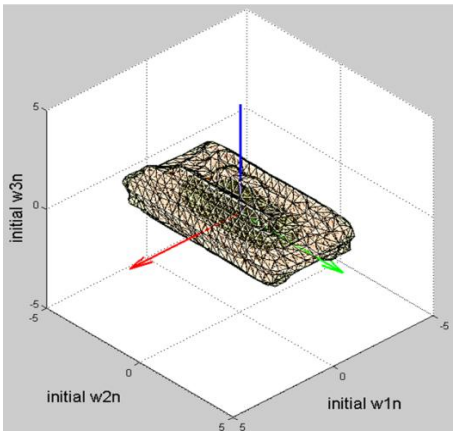

Fig.1. Isosurfaces in space of initial angular velocities for laser-scanned model of solar panel. See text.

Dividing the components of **L** by the principal inertia components gives the initial components of the angular velocity. Fig.1 shows isosurfaces of equally probable initial angular velocity vectors, generated using Eq.1 and computed numerically for a solar panel fragment that was scanned at JSC. Three semi-transparent isosurfaces are plotted. The most notable result is that the isosurfaces of probability density have shapes that roughly approximate triaxial ellipsoids with (decreasing) major axes in the directions of ω_2, ω_1, and ω_3, respectively. Therefore, the distribution of probable initial angular velocities favors large values of ω_2, and smaller values of ω_1 and ω_3, so the most likely initial state is one that has a large component of angular velocity along the intermediate axis of inertia. Interestingly, when the ω_2 component is large relative to the others, the free rotation of the body will exhibit the most extreme variety of orientations over time – i.e., the largest amount of "tumbling" motion. Such motion samples the space of possible reflected intensities in the most diverse manner (though still far from randomly) over a time period spanning numerous rotations (see sections 5 and 6). Thus, unless these results are otherwise affected by influences such as internal friction, magnetic retarding torque, and/or solar radiation torque, it seems initially possible that the distribution of object orientations may be approximated as random. However, it is seen below that even without such influences this is a relatively poor approximation.

3. Quaternion representation of orientation and intensity

The unit quaternion is a mathematical construction that represents an extension of the complex plane to four dimensions. Discovered by R. W. Hamilton in 1843 [4], the unit quaternion **z** can be used to represent the set of all axis-angle rotational orientations in a seamless, singularity-free manner, according to the following equation:

$$\bar{z} \equiv x_1\hat{i} + x_2\hat{j} + x_3\hat{k} + x_4 = n_1 \sin(\frac{\varsigma}{2})\hat{i} + n_2 \sin(\frac{\varsigma}{2})\hat{j} + n_3 \sin(\frac{\varsigma}{2})\hat{k} + \cos(\frac{\varsigma}{2}) \qquad (2)$$

where ς is the angle of rotation about the axis given by the unit vector **n**. The sum of the squares of the components is unity, so the unit quaternion represents the surface of a 4D hypersphere, known as S3 by mathematicians. Because of this constraint, the **i**, **j**, and **k** components are sufficient to completely define all possible orientations. Just as a 3D spherical surface can be projected onto two dimensions in a polar stereographic projection map without losing the information recorded on a hemisphere, so the unit quaternion can be projected onto a 3D spherical volume (hereafter the "orientation sphere"), thus allowing an immediate visualization of all possible rotation states. By dividing this volume into tiles of equal "3-area", a database of equally likely

orientations can be easily constructed. Orientations of objects are defined here by the directions of their principal axes of inertia ($I_1 < I_2 < I_3$) relative to an inertial coordinate system where the x-axis is from the debris object toward the observer, and the observer, object and the sun lie in the (x,y)-plane. The maximal diffuse and specular reflected intensities (i.e. for reflectivities of unity) at the centers of each volume element are generated for a chosen debris object, and these values may be mapped as points with varying colors as shown in Fig.2. Linear combinations of these two databases are used to model objects with both specular and diffuse characteristics. The orientation sequence of objects undergoing rotations may be plotted as trajectories through the spherical volumes. The yellow trajectory shown in the figure is a simple 360-degree rotation about a fixed axis. When starting from the orientation where the body and inertial coordinate systems are coincident, rotations about the x,y, and z (inertial) axes all fall on the green, red and blue diametric lines, respectively, and the surface of the sphere represents rotations of 180 degrees about all possible fixed axes.

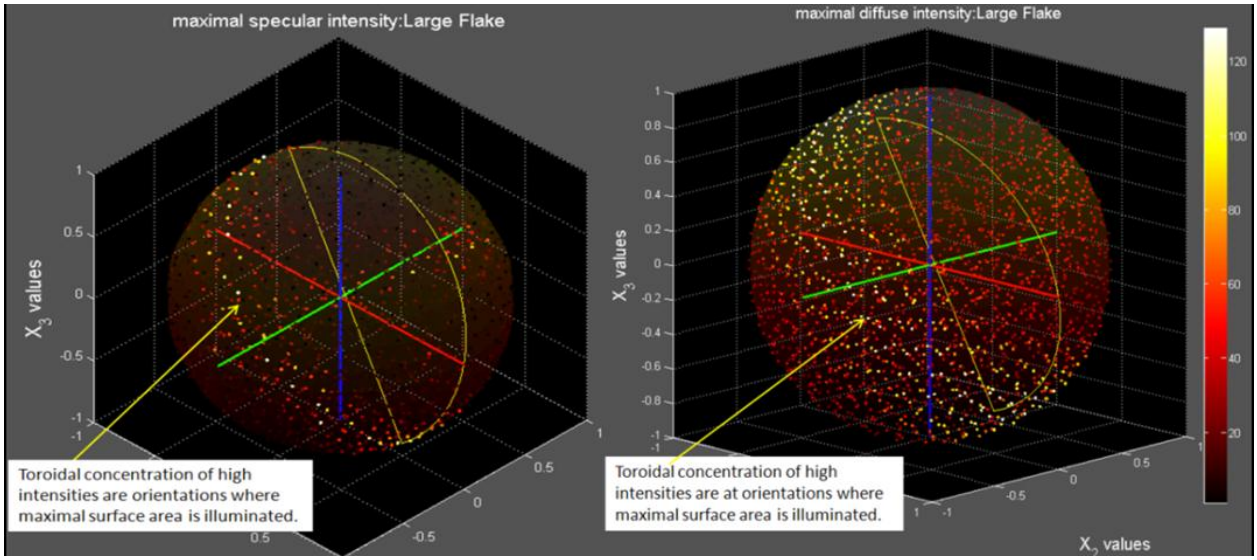

Fig.2: Specular and diffuse reflection databases for the SOCIT4:252.A1 flake, plotted on quaternion orientation sphere.

4. Solar radiation torque

The collective effects on rotation states of specular and diffuse reflection of solar radiation, as well as of thermal emission are collectively known as the Yarkovsky-O'Keefe-Radzievskii-Paddock effect (YORP) [cf.5]. The spin-altering effects of YORP have been verified observationally for small asteroids [6] and satellites [cf.7] and it has long been believed to be the source of rotational bursting – a phenomenon whereby small meteoroids spin-up to such a degree that centrifugal forces can cause catastrophic fragmentation [8] in ~10^5 years. Not surprisingly,

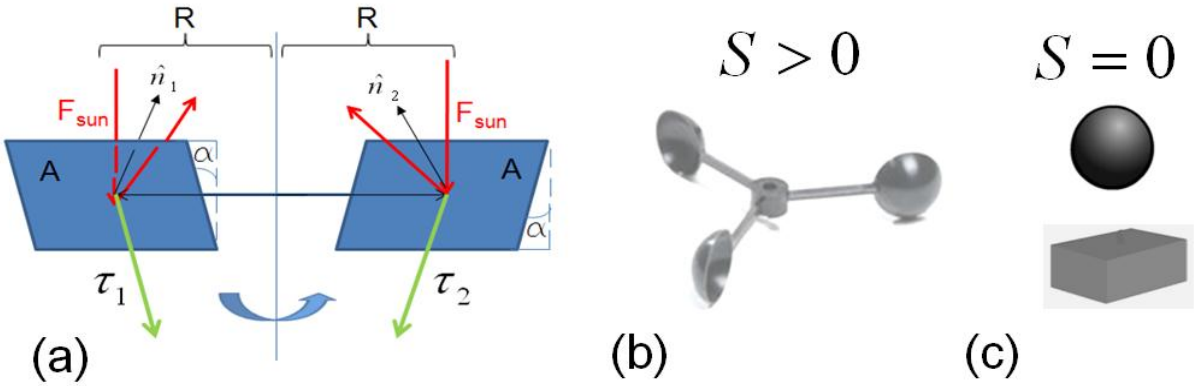

Fig. 3: (a) Simple object which experiences solar torque. (b) windvane (c) sphere and rectangular solid.

YORP can also be shown to have very significant effects on rotating space debris. In Fig.3a, a simple object is shown, composed of two plates of area A whose centers are separated by a distance 2R, and which have unit normal vectors as shown. The planes of the two plates are tilted as shown by an angle α with respect to vertical. Solar radiation is incident in the downward direction. For simplicity, the plates have only specular reflectivity given by ρ, and thermal emission is ignored. In this geometry the reflection of solar flux F_{sun} off of each plate yields torques τ_1 and τ_2 as shown. By adding these torques vectorially, the magnitude of the total torque is easily computed, but a more general expression is given below.

Debris objects in general experience a solar torque that is dependent on shape and variegation, but only shape effects are considered here. A uniform sphere or rectangular solid as shown in Fig.3c will experience no solar torque, while a windvane (b) will experience a relatively large solar torque. In general, for an object described by planar facets, the torque due to specular and diffuse reflection and thermal emission is written:

$$\bar{\tau}_s = \frac{-F_s A_{tot} \bar{r}}{c} \sum_{j, \hat{n}_j \cdot \hat{n}_s > 0} \left(\hat{n}_j \cdot \hat{n}_s\right) A_{jn} \bar{r}_{jn} \times \left\{ \left(\rho_D + \alpha\right)\left(\hat{n}_s + \frac{2}{3}\hat{n}_j \right) + 2\rho_S \left(\hat{n}_j \cdot \hat{n}_{sun}\right)\hat{n}_j \right\} \quad (3)$$

where A_{tot} and $\bar{r}$ are the total surface area and average distance from center of mass to a facet, while A_{jn} and r_{jn} are the facet areas and radii from the center of mass to the center of the jth facet, normalized by A_{tot} and $\bar{r}$, respectively. F_s, c, ρ_D, ρ_S and α are the solar flux (1370 W/m^2,[9]) , the speed of light, the diffuse and specular reflectivities, and the thermal absorptivity. For simplicity, Eq.3 assumes a state of thermal equilibrium with incident radiation for each facet at all times. This is equivalent to the assumption of zero thermal conductivity and is known as Rubincam's approximation [cf. 7]. $\hat{n}_j$ and $\hat{n}_S$ are the unit normal vector of the jth facet and the unit sun-direction vector. The characteristic time T_s over which the solar radiation torque can be expected to greatly change the angular momentum of a debris object is simply the characteristic angular momentum $I_3\omega_0$ divided by the torque given in Eq.3. If I_3 is taken to be roughly that of a disk, the result is

$$T_s \cong \frac{\omega_0 c I_3}{F_S A_{tot} \bar{r} S} \cong (32hrs)\left(\frac{m}{1gm}\right)\left(\frac{1cm^2}{A_{tot}}\right)\left(\frac{1\min}{P}\right)\left(\frac{1}{S}\right) \quad (4)$$

where P, m, and S are the initial rotation period, the mass, and the magnitude of the vector sum in Eq.3. For objects with no *windvanedness*, such as the sphere or rectangular solid in Fig.3, S=0 and T_s goes to infinity, while irregular objects commonly have S >1. For example, for the synthetic pinwheel described below, S is considerably larger than unity. Eq.4 indicates that if such objects are of centimeter scale with mass on the order of grams and rotation rates on the order of minutes, their angular momentum can change by a large percentage within hours. The object shown in Fig.4a is a synthetic pinwheel -- a simple object with obvious solar torque characteristics. Eq.3 was used to compute the solar torque, in the body coordinate system, acting on this object as a function of the direction of the sun, where for simplicity, pure specular reflectivity was assumed and α =0. Each vector on the surrounding sphere illustrates the magnitude and direction of the solar torque for the case where the sunlight is incident from the direction indicated by the location of the vector relative to the object center. The pinwheel exhibits a dipole-like distribution of solar torque. Where the vectors point outward, the solar torque causes increase in angular momentum about the corresponding body-direction, which is true as expected if the sun is on the symmetry axis. Fig.4b illustrates the corresponding torque for a flake-like object created by the SOCIT4 satellite break-up test, designated SOCIT4:252.A1. This object is a small (~2x1cm), Aluminum fragment. For this object (hereafter "the flake"), the torque field is more complicated, but nonetheless is a smooth function of sun direction.

5. Rotational dynamics in the presence of solar radiation

The Euler equations describe the evolution of the components of the angular velocity vector ω in the coordinate system of the body. With the external torque given by Eq.3, these equations may be written in nondimensional form as follows:

$$\frac{d\omega_{1n}}{dt_n} = \frac{\Delta_{23n}}{I_{1n}}\omega_{2n}\omega_{3n} + \frac{C_s}{I_{1n}}\tau_{sn1} \quad (5a)$$

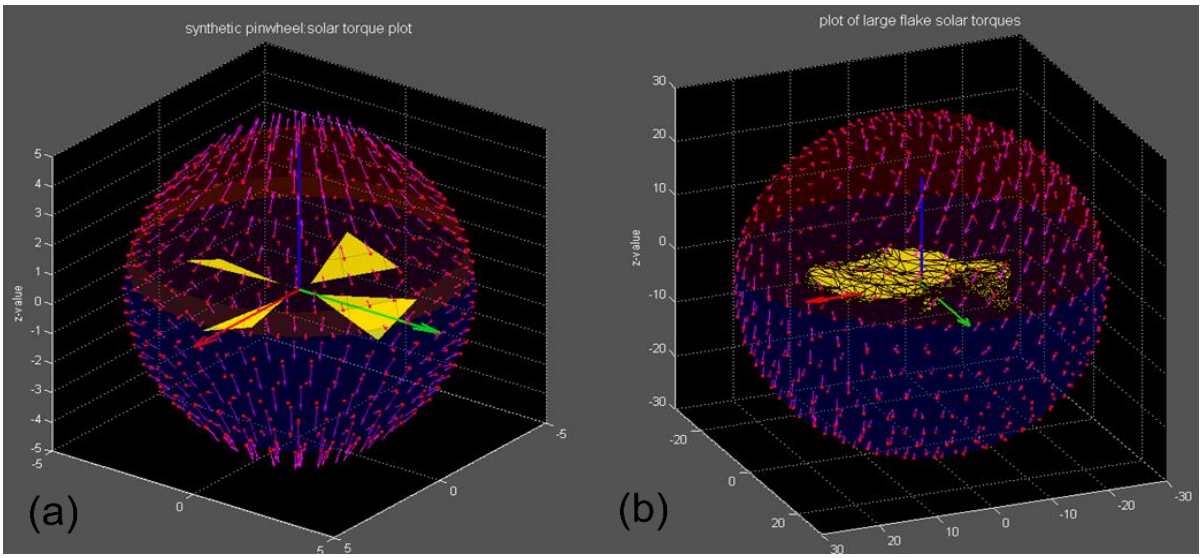

Fig.4: Synthetic pinwheel (a) and flake (b) with the corresponding solar radiation torques due to pure specular reflection.

$$\frac{d\omega_{2n}}{dt_n} = \frac{\Delta_{31n}}{I_{2n}}\omega_{1n}\omega_{3n} + \frac{C_s}{I_{2n}}\tau_{sn2} \tag{5b}$$

$$\frac{d\omega_{3n}}{dt_n} = \frac{\Delta_{12n}}{I_{3n}}\omega_{1n}\omega_{2n} + \frac{C_s}{I_{3n}}\tau_{sn3} \tag{5c}$$

where the $\omega_{jn} \equiv \omega_j / \omega_0$, $\Delta_{ijn} \equiv \left(I_i - I_j\right)/I_3$, $I_{in} \equiv I_i / I_3$, C_s is a constant and time is in units of the reciprocal of the initial angular velocity ω_0. Terms representing internal friction and magnetic retarding torque may be added to the above equations, but they are not included in the work presented here.

The nondimensional rates of change of the components x_i of the unit quaternion are only dependent on the x_i-values and the components of ω as defined above [10], according to:

$$\frac{dx_1}{dt_n} = \frac{1}{2}\left(\omega_{1n}x_4 + \omega_{3n}x_2 - \omega_{2n}x_3\right) \tag{6a}$$

$$\frac{dx_2}{dt_n} = \frac{1}{2}\left(\omega_{21n}x_4 - \omega_{3n}x_1 + \omega_{1n}x_3\right) \tag{6b}$$

$$\frac{dx_3}{dt_n} = \frac{1}{2}\left(\omega_{3n}x_4 + \omega_{2n}x_1 - \omega_{1n}x_2\right) \tag{6c}$$

$$\frac{dx_4}{dt_n} = \frac{1}{2}\left(-\omega_{1n}x_1 - \omega_{2n}x_2 - \omega_{3n}x_3\right) \tag{6d}$$

Equations 5a-c and 6a-d are integrated as a set, using an 8th order Runge-Kutta routine . Results are presented in the following section.

6. Dynamical evolution of specific objects.

Fig.5 shows the dynamical results of the integration of Eqs.5 and 6, for the case of the symmetric pinwheel described above. The pinwheel was given an area-to-mass value characteristic of multi-layer insulation (hereafter MLI), of 2.0m^2/kg, and has a maximum diameter of 7.0cm. In this case, the initial rotation period is 2.5 minutes, and the component of the angular velocity along the I_2-axis of inertia was largest, which is a likely initial condition considering the results of section 2. I_2=I_1 in this case, and time is in units of $1/\omega_0$, spanning approximately an interval of four hours. Fig 5a shows the trajectory of the angular momentum **L** (red) and angular velocity ω (blue) in the frame of the body. As is to be expected, both vectors precess about the I_3 body-axis, while ω_0 precesses about **L**. Both vectors grow in magnitude, spiraling upward, then spiral downward as they shrink. Fig.5b shows the same trajectory in inertial space, indicating a large increase and subsequent decrease in both vector magnitudes. Notably, **L** reaches a magnitude of three times its initial value, before approaching the initial conditions once again. Fig.5d shows the evolution of the components of these vectors over time. The components of **L** change relatively slowly, while ω components oscillate with the rotation period. Fig.5c is the trajectory of the I_3 body-axis in inertial space. The first ~1/2 of the trajectory is in black and the rest in green. Note the large change in character of this trajectory as time proceeds. Fig.5f shows the trajectory on the orientation sphere, where again the first part is in black. While the trajectory samples a large range of possible orientations, it does so in a manner that varies widely over differing portions of the full time interval. Fig.5e shows that the energy, in units of the minimum possible energy $L_0^2/2I_3$ given the initial angular momentum $\mathbf{L_0}$, changes by a factor of ~6 between maximum and minimum values over the entire time interval.

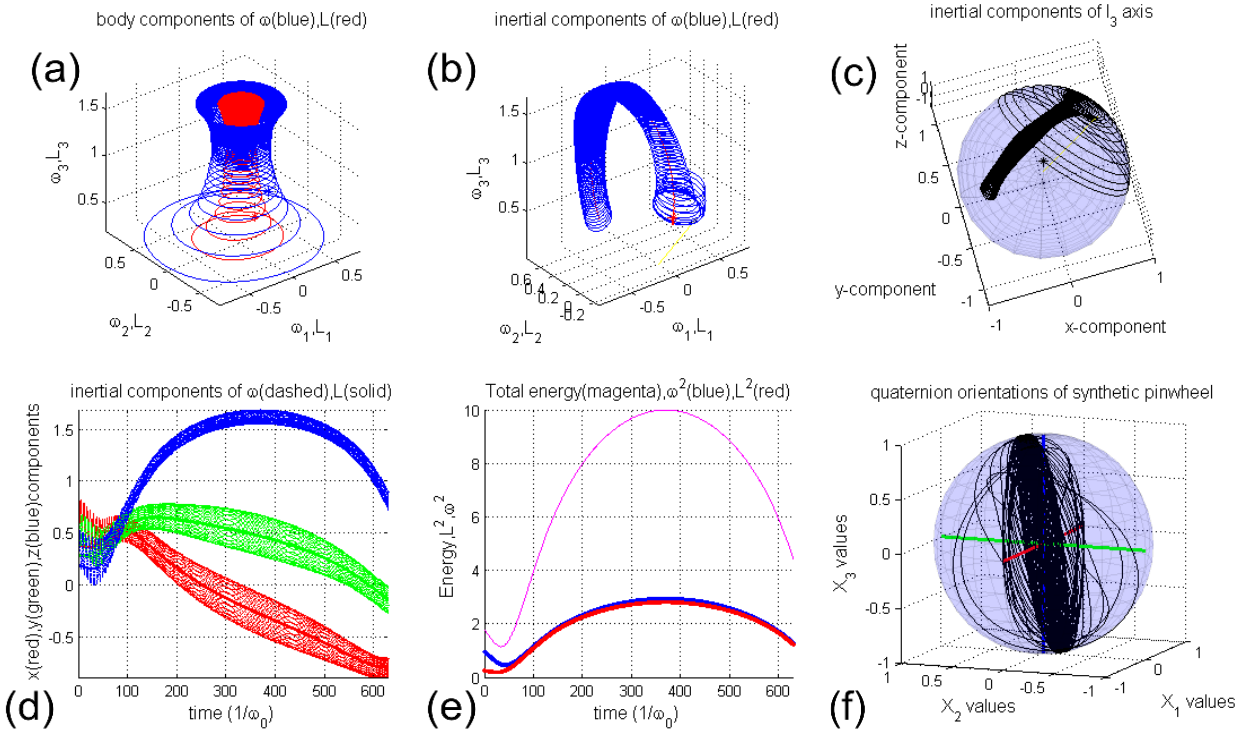

Fig.5. Dynamical evolution of synthetic pinwheel. See text.

Fig.6 shows the dynamical results for the pinwheel described above, but in this case the principal moments of inertia were artificially set to distinctly triaxial values (I_1/I_3=.21, I_2/I_3=.65). All other conditions are the same as in Fig. 5. Since most objects will probably be triaxial, this case may represent an object of typical dimensions, but with a relatively large windvanedness. Initially, ω and **L** precess about the I_3 body-axis, but as the evolution proceeds, energy is added by solar radiation, such that the higher energy state (for a given L) of precession of ω and L about

the I_1 body-axis is entered. This represents crossing of a dynamical separatrix between these two well-known states of free rotation [8]. At this point, the character of the rotation state changes drastically (cf. Fig.6d), which causes large changes in the nature of the light curve as well, as shown in the next section. The first half of the I_3 body-axis

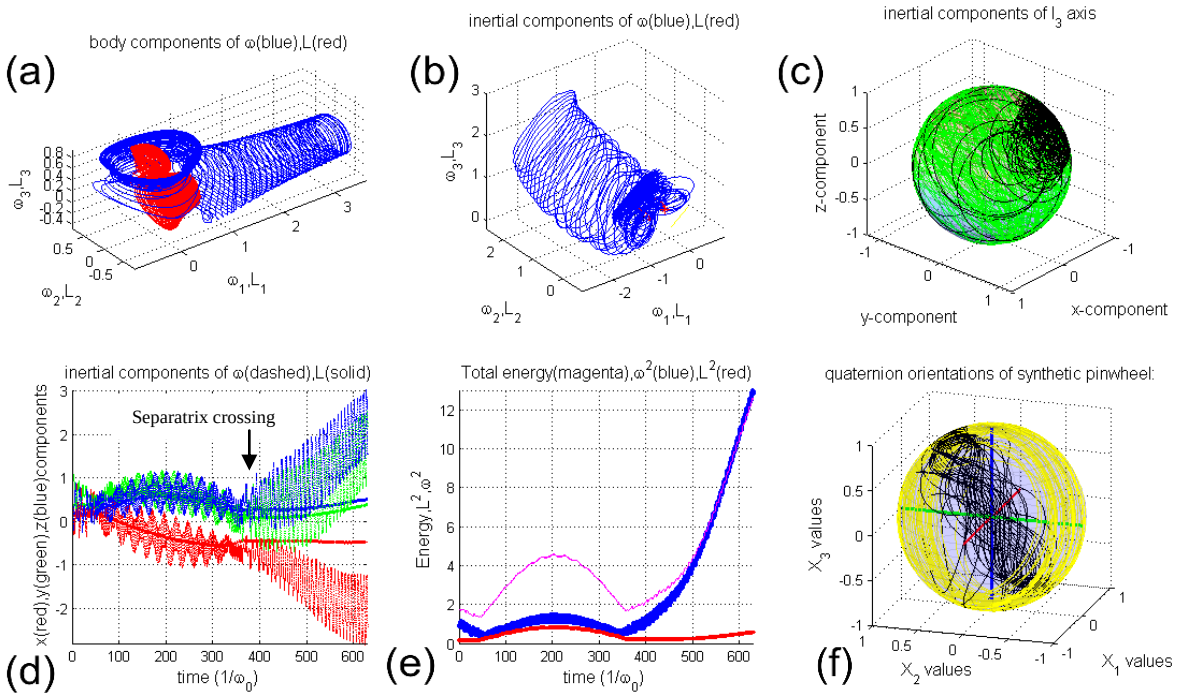

Figure 6. Dynamical evolution of asymmetric pinwheel. See text.

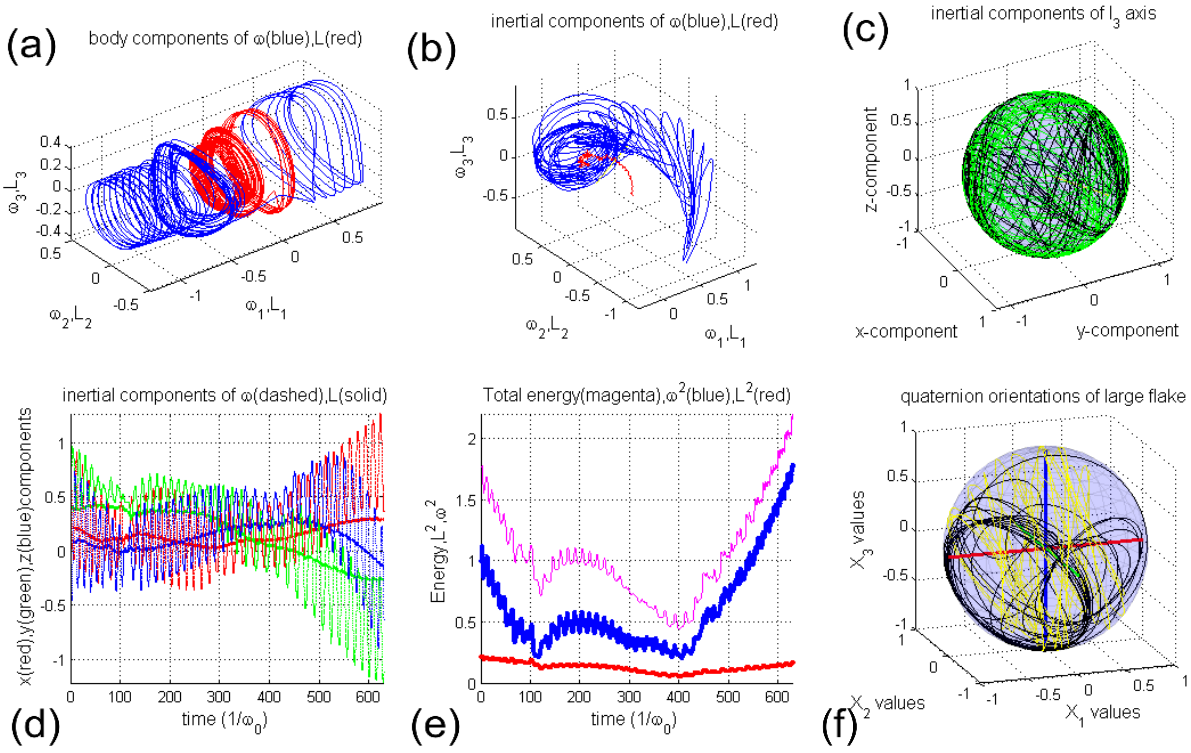

Fig.7. Dynamical evolution of the flake. See text.

trajectory in inertial space (Fig.6c) and the orientation sphere trajectory (Fig.6f) are again highlighted in black, to indicate the difference in orientations between the first and second halves of the simulation. While these trajectories sample a large range of the possible states, they clearly do so in a manner that varies widely between the first and second halves of the full time interval.

Fig.7 shows the dynamical results for the flake described above (see Fig 4b). All other conditions are the same as in Fig.6. The components of the inertia tensor were computed using the faceted model from the laser scan and processing performed at JSC. In this simulation ω and **L** first precess about the positive I_1 body-axis, then along the negative I_1 body-axis. During this time, the total energy fluctuates by over a factor of ~4 from minimum to maximum. Once again ,the first half of the quaternion and I_3 body-axis orientation trajectories are highlighted in black. Midway through the simulation, the rotation state changes from free precession about the positive I_1-axis to free precession about the negative I_1-axis. As a result, the orientations sampled during the second half of the total time differ considerably from those of the first half, in which the trajectory approximates a repeating small circle near the surface of the orientation sphere.

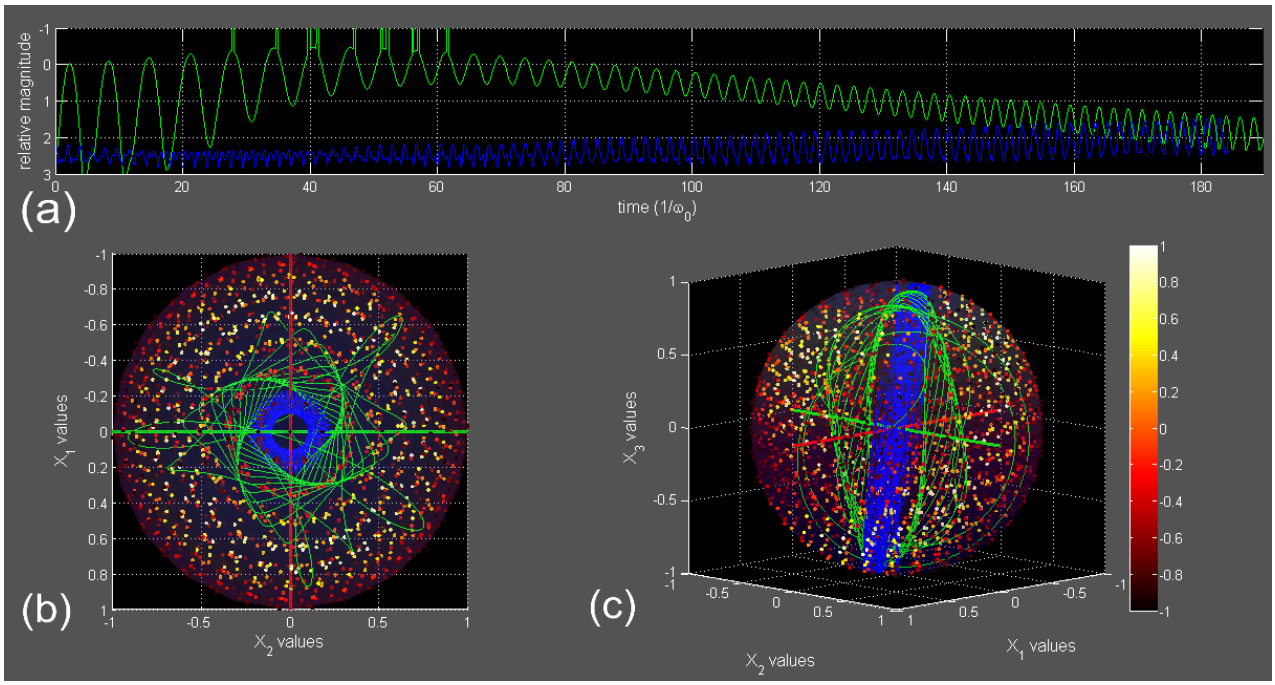

Fig.8: Light curves and orientations corresponding to Fig.5, synthetic pinwheel. See text.

7. Effects of dynamical evolution on light curves

Fig. 8a shows the relative visual magnitude versus time corresponding to two portions of the synthetic pinwheel dynamical evolution shown in Fig.5. The green and blue trajectories each represent approximately 75 minutes of the earlier and later portions of the evolution, respectively. Fifty percent Lambertian diffuse and fifty percent specular reflectivity were assumed for each case shown in this section. Near the beginning of the green light curve, several specular reflection events occur, each increasing the brightness by approximately three magnitude units (a factor of ~20 in intensity), which exceeds the scale limits of the graph. Figs 8b and 8c are different views of the trajectories on the orientation sphere for the same portions of the time evolution, with the diffuse quaternion intensity database shown as color-coded points as described in section 2. Note that the green trajectory generally samples portions of orientation space that are farther from the center of the sphere, while the blue trajectory remains close to the x_3 inertial axis (i.e. the vertical axis). Physically, this means the blue trajectory involves states that are relatively close to pure rotations about this axis. This can also be noted in Fig.5d, where large values of ω_3 are seen to develop in inertial space. The primary periodic modulation in the visual magnitude of the green curve corresponds to the rotation period, which changes by a factor of ~2 over the entire dataset. In the blue light curve, the rotation period

beats against the free precession period, which is comparable to the rotation period. This produces a more complex waveform. Interestingly, Fourier analysis of a light curve of this form would yield two frequencies, the ratio of which is a measure of the magnitude of the difference between the principal components of inertia.

Fig.9b shows relative visual magnitude versus time corresponding to two portions of the dynamical evolution of the triaxial synthetic pinwheel as shown in Fig.6, while Fig.9a shows the same data on a plot of relative intensity rather than magnitude, in order to better demonstrate the differences between the two light curve segments. As in Fig.8, the green and blue trajectories each represent approximately 75 minutes of time, earlier and later in the numerical integration interval, respectively. The blue curve in Fig.9b has been artificially raised by two magnitude units to promote separation between the curves. The green curve primarily represents a rotation state with ω and L vectors precessing about the I_3-axis, whereas the blue curve represents the rotational evolution after the crossing of the separatrix into a state of rotation about the minimum axis of inertia. Again, note the large difference in the regions of orientation space sampled by the two trajectories in Fig.9c and 9d, and the consequent differences in the light curve sequences. The green trajectory passes repeatedly near the center of the orientation sphere, while the blue remains close to the sphere's surface. Also note that specular reflections, identifiable by sudden increases and decreases in brightness, usually occur at the crests of the smooth, diffuse reflections which characterize the bulk of the light curve data, which should be generally true for roughly flat objects.

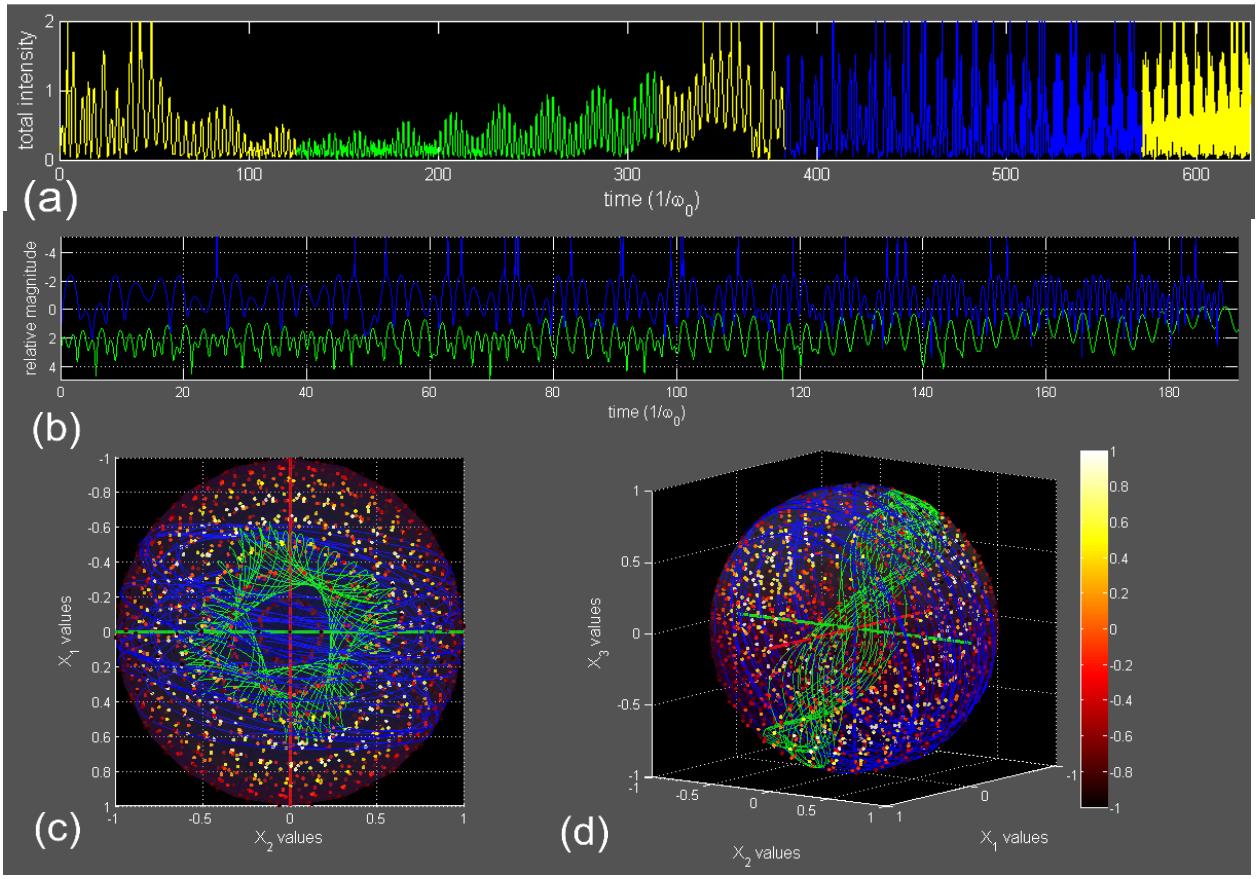

Fig.9. Light curves and orientations for triaxial pinwheel sequence. See text.

Fig.10 shows the light curve of the flake during the rotational evolution seen in Fig.7. Once again it is evident from the lower panels (10b, 10c) that the green and blue portions of the evolution sample very different regions of orientation space. The green trajectory, representing precession of the ω and L vectors about the positive I_1 body-axis, cycles approximately on a small circle on the outer surface of the orientation sphere, whereas the blue (later) trajectory samples a broader range of orientations, while precession occurs around the negative I_1 body-axis**.** As in other cases described above, the resulting light curve data for the first and second parts of the evolution are markedly different in character.

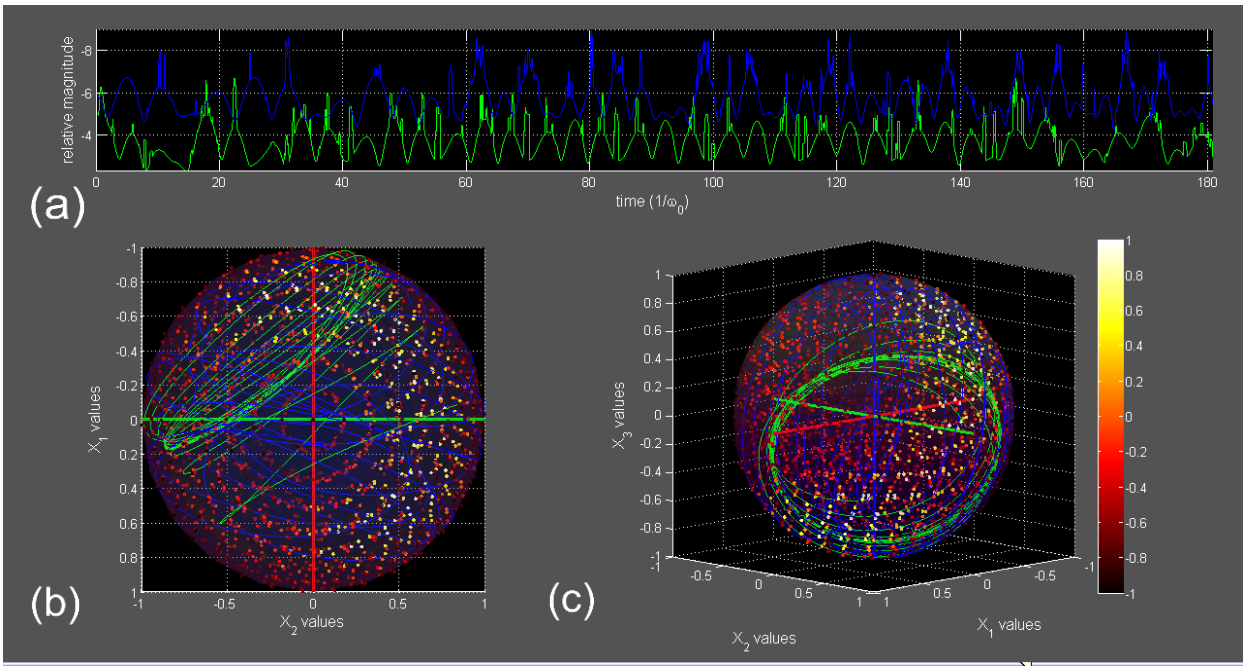

Fig.10. Lightcurves and orientations for flake rotation sequence. See text.

8. Discussion and conclusions

It is most probable for space debris objects that a large component of the initial angular velocity will be directed along the intermediate axis of inertia. Under such conditions, ω for freely rotating, significantly triaxial and irregular debris objects will change markedly within a single rotation period, illustrating the extreme importance of realistic rotational evolution to be considered when attempting to divine object shape and compositional properties from unresolved light curves. Additionally, the torque acting on small debris objects due to solar radiation must be considered in any realistic analysis. To this end, the rotational dynamics of one idealized and one probably realistic piece of centimeter-scale space debris under the influence of solar radiation torque have been examined here. The results reveal very significant effects, with large changes in **L** occurring within hours for these objects when the initial rotation period is on the order of minutes. As illustrated by Eq. 4, the time required for large relative changes in **L** scales inversely as the the rotation period, so that for periods on the order of seconds, major changes in **L** will take typically several days to occur. The effects increase with area-to-mass ratio, and require irregularityof shape and/or reflectivity, vanishing for uniform spheres or uniform rectangular solids. For typical objects, it is interesting to note that a state of free rotation (and consequent precession) can be assumed over a few rotation periods, while solar radiation changes **L** and hence the particular character of the free rotation, over a somewhat longer timescale. Thus, over short time intervals, the well-known states are observed in which ω precesses about **L** in inertial space, and where ω and **L** precess about either the I_1 or I_3 axes in the body coordinate system. There are no rotation states that randomly sample orientation space within a few rotation periods, and even over many rotation periods, observation sequences will generally not be represented well by a random subset of all possible orientations. Under solar radiation alone, L appears to vary chaotically, with extreme dependence on initial conditions, although a continuum of initial conditions should be examined in order to identify any possible patterns in eventual rotation states of debris objects. It seems likely that some small debris that have been in orbit for years may be rotating very rapidly. Finally, the presence of internal friction and magnetic damping should be considered in future studies. It is believed that these effects, when significant relative to solar radiation, may lead to preferred rotation states and a consequent reduction in the suite of likely eventual rotation states.

9. References

1. Schildknecht, T., Musci, R., and T. Flohrer (2007). Challenges related to discovery, follow-up, and study of small high area-to-mass ratio objects at GEO. Proceedings of the Advanced Maui Optical and Space Surveillance Technologies Conference, Wailea, Maui, Hawaii, September 2007, pp.354-359.

2. Schildknecht, T., Musci, R.,Fruh, C., and M. Ploner (2008), Color Photometry and Light Curve Observations of Space Debris in GEO, Proceedings of the Advanced Maui Optical and Space Surveillance Technologies Conference, Wailea, Maui, Hawaii, September, 2008.

3. Cowardin, H., Abercromby, K., Barker, E., and T. Schildknecht (2010). Characterization of Orbital Debris Photometric Properties Derived from Laboratory-Based Measurements. Proceedings of the Advanced Maui Optical and Space Surveillance Technologies Conference, Wailea, Maui, Hawaii, September, 2010.

4. Hamilton, W.R. (1844–1850), *On Quaternions; or on a new System of Imaginaries in Algebra*, appeared in 18 installments in volumes xxv–xxxvi of The London,Edinburgh and Dublin Philosophical Magazine and *Journal of Science* (3rd Series).

5. Bottke, W.F., Vokrouhlicky, D., Rubincam, D.P., and D. Nesvorny (2006), The Yarkovsky and YORP effects: Implications for asteroid dynamics, *Ann.Rev. Earth Planet. Scoi.* 34, 157-191.

6. M. Kaasalainen et al. (2007): Acceleration of the rotation of asteroid 1862 Apollo by radiation torques. *Nature* 446, 42-0.

7. D.P. Rubincam (1995). Asteroid orbit evolution due to thermal drag. *J. Geophys Res.* 100, 1585-1594.

8. Paddack, S.J. (1969). Rotational Bursting of Small Celestial Bodies: Effects of Radiation Pressure. *J. Geophys. Res.* 74, No. 17, pp. 4379-4381.

9. Kopp, G., Lawrence, G., and Rottman, G., "The Total Irradiance Monitor (TIM): Science Results," *Solar Physics*, 230, 1, Aug. 2005, pp. 129-140.

10. Baruh, Haim (1998) *Analytical Dynamics*, McGraw-Hill Science Engineering, New York.

11. Efroimsky, M. (2001) Relaxation of wobbling asteroids and comets – theoretical problems, perspectives of experimental observation, *Planetary and Space Science* 49, 937-955.